

IPMC-Based Purcell's Three-Link Swimmer Simulations and Experiments at Low-Reynolds Conditions

Nuevo-Gallardo, Cristina; Tejado, Inés; Hunt, Andres; Vinagre, Blas M.

DOI

[10.3390/act13120498](https://doi.org/10.3390/act13120498)

Publication date

2024

Document Version

Final published version

Published in

Actuators

Citation (APA)

Nuevo-Gallardo, C., Tejado, I., Hunt, A., & Vinagre, B. M. (2024). IPMC-Based Purcell's Three-Link Swimmer: Simulations and Experiments at Low-Reynolds Conditions. *Actuators*, 13(12), Article 498. <https://doi.org/10.3390/act13120498>

Important note

To cite this publication, please use the final published version (if applicable).
Please check the document version above.

Copyright





Other than for strictly personal use, it is not permitted to download, forward or distribute the text or part of it, without the consent of the author(s) and/or copyright holder(s), unless the work is under an open content license such as Creative Commons.

Takedown policy

Please contact us and provide details if you believe this document breaches copyrights.
We will remove access to the work immediately and investigate your claim.

Article

IPMC-Based Purcell's Three-Link Swimmer: Simulations and Experiments at Low-Reynolds Conditions

Cristina Nuevo-Gallardo ^{1,*} , Inés Tejado ^{1,*} , Andres Hunt ²  and Blas M. Vinagre ¹ ¹ Escuela de Ingenierías Industriales, Universidad de Extremadura, 06006 Badajoz, Spain; bvinagre@unex.es² Faculty of Mechanical Engineering, Delft University of Technology, 2628 Delft, The Netherlands; a.hunt@tudelft.nl

* Correspondence: cnuevog@unex.es (C.N.-G.); itejbal@unex.es (I.T.); Tel.: +34-924489767 (I.T.)

Abstract: The Purcell's swimmer, consisting of three links with two one-degree-of-freedom joints as defined by Edward M. Purcell, has been studied by several authors since its introduction in 1977. Researchers have delved into its mathematical foundations, analysing and optimising its motion for efficient propulsion. However, despite these theoretical advances, the practical realisation and experimental characterisation of Purcell's swimmers remains relatively unexplored. Critical aspects such as material selection, manufacturing techniques, and experimental validation under real conditions represent important knowledge gaps. This paper contributes to bridging this gap by presenting a prototype of such a swimmer using ionic polymer-metal composites (IPMC) as link actuators. A simulation model is developed based on physical modelling tools in MATLAB®/Simulink®. Both simulation and experimental results at low-Reynolds-number (Re) conditions are presented to demonstrate the performance of the swimmer.

Keywords: low-Reynolds number; Purcell's swimmer; modelling; flexible; IPMC; prototype



Citation: Nuevo-Gallardo, C.; Tejado, I.; Hunt, A.; Vinagre, B.M. IPMC-Based Purcell's Three-Link Swimmer: Simulations and Experiments at Low-Reynolds Conditions. *Actuators* **2024**, *13*, 498. <https://doi.org/10.3390/act13120498>

Academic Editor: George Knopf

Received: 16 September 2024

Revised: 25 November 2024

Accepted: 2 December 2024

Published: 5 December 2024



Copyright: © 2024 by the authors. Licensee MDPI, Basel, Switzerland. This article is an open access article distributed under the terms and conditions of the Creative Commons Attribution (CC BY) license (<https://creativecommons.org/licenses/by/4.0/>).

1. Introduction

Innovative advances in miniature artificial devices are revolutionising healthcare by enabling applications such as minimally invasive treatments, targeted drug delivery, and diagnosis [1]. Designed to navigate through complex biological environments, these microscopic robots face significant challenges in locomotion, fabrication, and power supply, among others [2]. At the microscale, characterised by a low Reynolds number (Re), fluid dynamics fundamentally differ from macroscopic scales. In this regime, viscous forces outweigh inertial ones, significantly impacting locomotion. The “scallop theorem” illustrates this challenge: organisms with a single degree of freedom, such as a clam, are unable to generate net displacement in low- Re environments due to the symmetric nature of their movements. Consequently, asymmetric or non-reciprocal motions are essential for effective propulsion at this scale.

Edward M. Purcell made significant contributions to addressing these challenges in his 1977 review on microscale navigation techniques [3]. His paper proposed three different navigation methods or swimmers, with so-called Purcell's swimmer being the simplest ‘animal’ capable of moving in these fluid regimes. This swimmer consists of three segments and two joints, similar to a “boat with oars at both ends”. The lateral segments can rotate in sequences that must be asymmetric to achieve net movement. These sequences, known as motion primitives or gaits, define the angular positions of the lateral segments by piecewise functions.

Since Edward M. Purcell introduced the concept of Purcell's swimmer, numerous researchers have studied its properties. Studies focusing on its kinematics and dynamics have been published from the early 2000s up to the present. Concerning dynamic models, two-dimensional models have been developed and analysed in [4–11], in addition to the study of the parameters that influence the displacement of the swimmer, including its

geometry [4,8,10], the motion primitives [5], and its asymmetry and stability [7]. Other works studied the dynamics by means of a three-dimensional model of the swimmer [12,13], while others analysed, firstly, the dynamics of the generalised case of N-link and tried to approximate it to a sperm cell swimmer, and then apply the model to the three-link case [9]. With respect to the motion primitives, traditional gaits can be found in the literature, named square, circular, etc., which are implemented and compared in [12,14], while other methods for designing new motion primitives have also been reported in [5,8,15–21].

Regarding the type of actuator that rotates the lateral links, the most common ones that can be found in the literature are motors and magnetic fields. Two prototypes actuated by servomotors were fabricated in [14,22], while another motorised prototype was introduced in [23] although no experimental results are given. In relation to magnetic fields, magnetic Purcell's swimmers have been explored in studies such as [24–27], and a few-centimetre-long magnetic prototype was created and tested experimentally in [26]. Other authors have studied the influence of passive and active elastic joints [23,28] from a mathematical point of view.

Robot miniaturisation requires simple actuator structure and sufficiently large strains, characteristic to electroactive polymer transducers. Ionic polymer–metal composites (IPMCs) have been considered as alternative materials to design and simulate a three-link Purcell's swimmer in [29], while the same technology was used for the fabrication of an articulated three-link swimming robot in [30], identifying its dynamic model experimentally. Despite these works, IPMC technology has not yet been experimentally validated as suitable for Purcell's three-link swimmers.

In this context, this paper focuses on the use of IPMC technology and proposes a novel Purcell's swimmer prototype with IPMC actuators as joints and rigid segments, which was simulated and experimentally tested in low- Re regimes. The design of this prototype is described, along with the design and implementation of simulations in MATLAB®/Simulink®. In addition, experiments were carried out to validate the simulation results in terms of the displacement of the swimmer, considering two types of viscous fluids (water mixed with glycerine and water mixed with dishwashing detergent) in order to mimic the hydrodynamic conditions characteristic of the microscale.

In practice, the viability of a Purcell's swimmer depends on material capabilities, which are complex and impractical to capture in theory, and require experimental validation (addressed in combination in this work). This study aims to investigate the impact of joint flexibility of a Purcell's swimmer on its locomotion. While traditional models employ rotational joints that rotate at fixed angles provided by the motion primitives, this research proposes a novel approach by utilising IPMC actuators as flexible joints. These actuators, renowned for their high flexibility and rapid response, enable a more realistic emulation of biological movement. Through physical modelling-based simulations and experiments, this paper examines how IPMC joints affect the implementation of motion primitives and, consequently, the displacement of the swimmer in comparison with the classical model.

The innovative use of IPMC actuators offers significant opportunities for miniaturisation, opening doors for other potential applications [31,32]. By eliminating the need for waterproof enclosures required by traditional motorised systems, IPMCs allow for more compact and flexible designs. Furthermore, future research could lead to the development of fully soft robotic systems where all components, including the power source and sensors, are integrated into a flexible structure. Such a paradigm shift would lead to highly manoeuvrable and adaptable robots capable of navigating within complex environments and performing delicate tasks. Nevertheless, the implementation of this technology has been constrained by a number of challenges, including the complexity of their dynamic behaviour.

This document is organised as follows: Section 2 provides the theoretical framework necessary for understanding the interaction between the swimmer and the environment, alongside the modelling of Purcell's swimmers for low- Re environments and the definition of motion primitives. Section 3 outlines the methodology employed in this work, detailing the mechanical design of the fabricated IPMC-based Purcell's swimmer prototype, equipment used, simulation model, and testing procedures. The results of both simulations and

experiments are presented and discussed in Section 4. Finally, conclusions and future works are drawn in Section 5.

2. Theoretical Foundations

This section is devoted to the description of the main characteristics of the physical environment where the Purcell's swimmer would navigate at low- Re regimes.

2.1. Physical Environment

The study of hydrodynamics involves numerous effects or forces characteristic of the fluid that can affect the motion of a particle or object within the environment. In order to simplify these effects, certain dimensionless numbers that relate some effects to others have been defined (see [33]), and depending on their value, some of them can be neglected.

The dimensionless number considered in this work is Re , which relates viscous and inertial forces by means of the following expression:

$$Re = \frac{vl\rho}{\mu} \quad (1)$$

where v and l are the characteristic velocity and dimension, respectively (to be detailed later), and ρ and μ are the density and dynamic viscosity of the fluid, respectively. This expression is applied to Newtonian and incompressible fluids.

Depending on the value of Re , the fluid can be in a laminar or turbulent regime [33,34]. In the laminar regime with $Re > 1$, inertial forces predominate over viscous ones, whereas as Re decreases below 1, viscous forces have a greater influence on the medium. Consequently, Re is a critical parameter in fluid environments, as it governs the relative influence of inertial and viscous forces on particle dynamics, thereby affecting particle motion.

The number Re must be calculated depending on the item to be analysed. For instance, in order to study the motion of a particle in the fluid, which is the aim of this work, the velocity used to calculate Re would be the relative velocity of the particle with respect to the fluid, while the characteristic length would be that of the particle. Thus, a different Re regime can be achieved modifying the dimensions of the moving particle or the environment, as seen in Table 1, where values of Re for different situations at the micro- and macroscale are shown. Similar regimes to the microscale can be achieved when selecting the appropriate fluid at the macroscale (as is the case of the pool filled with silicon oil) or by considerably decreasing the size of the swimmer (see the case of the small swimmer in a pool filled with water).

Table 1. Values of Re for different vessels of the cardiovascular system and macroscale pools, considering swimmers moving within the environment (based on [35]). The following classification with respect to Re was considered: low (laminar regime governed by viscosity), medium (laminar regime not governed by viscosity), and high (turbulent regime).

Environment	Density (kg/m ³)	Dynamic Viscosity (Pa·s)	Length (m)	Velocity (m/s)	Re	Regime
Swimmer in aorta	1070	3.5×10^{-3}	10^{-6}	0.4–0.04	0.11–1	Low
Swimmer in capillary	1070	3.5×10^{-3}	10^{-6}	10^{-4} – 10^{-5}	3×10^{-4} – 31×10^{-4}	Low
Swimmer in pool * filled with water	1000	1.002×10^{-3}	3×10^{-2}	3.3×10^{-3}	98.80	Medium
Swimmer in pool * filled with silicon oil	964	0.0964	3×10^{-2}	3.3×10^{-3}	0.99	Low
Small swimmer in pool * filled with water	1000	1.002×10^{-3}	3×10^{-3}	3.3×10^{-4}	0.98	Low

* The pool has been considered of dimensions 3×5 m.

2.1.1. Hydrodynamics in Low-*Re* Regime

In the study of hydrodynamics in a fluid, the Navier–Stokes equations are essential for this analysis, which define the forces that appear in a moving fluid with certain velocity. The expression for a Newtonian and incompressible fluid is [36,37]

$$\rho \frac{D\mathbf{v}}{Dt} = -\nabla p + \mu \nabla^2 \mathbf{v} + \rho \mathbf{f} \quad (2)$$

where D/Dt is the material derivative, defined as $\left(\frac{\partial}{\partial t} + \mathbf{v} \cdot \nabla\right)$. The term $\rho \frac{D\mathbf{v}}{Dt}$ represents the inertial effects, ∇p is the pressure gradient present in the fluid, $\mu \nabla^2 \mathbf{v}$ denotes the diffusion and internal forces, and \mathbf{f} are other external forces typically arising from the action of gravity [36].

Equation (2) can be dimensioned according to certain parameters. In this case, to better appreciate the inertial and viscous effects, it can be rewritten as a function of *Re* as follows:

$$Re \frac{D\mathbf{v}}{Dt} = -\frac{Re}{\rho} \nabla p + \nu \nabla^2 \mathbf{v} + Re \mathbf{f} \quad (3)$$

In cases where *Re* is less than 1, which occurs at the microscale, a situation called slow viscous flow has to be considered due to the viscous forces resulting from shearing motions of the fluid. These forces predominate over the inertial ones associated with the acceleration or deceleration of fluid particles [36]. According to the above, both the inertial terms and the gravity contribution in (3) could be omitted since, on the one hand, they depend only on *Re*, and this number will take a very small value; on the other hand, these terms depend on the acceleration, which is negligible in these regimes [37]. Thus, Navier–Stokes Equation (2) can be transformed into the Stokes equation, defined as [36]

$$\mu \nabla^2 \mathbf{v} = \nabla p \quad (4)$$

Conversely, the law of conservation of mass can be applied to any stationary volume element within a flowing fluid [36], resulting in the equation of continuity:

$$\frac{\partial \rho}{\partial t} = -\nabla \cdot (\rho \mathbf{v}) \quad (5)$$

For an incompressible fluid, this equation can be simplified to $\nabla \cdot \mathbf{v} = 0$, where $\nabla \cdot \mathbf{v}$ is the net rate of flux. This simplification, along with the Stokes equations, establishes the creeping motion equations for a low-*Re* regime [36].

As it can be deduced from their expression, Stokes equations are characterised by being linear and time-independent, which implies two important properties of this type of flow:

1. Rate independence: When a swimmer implements a specific sequence of movements, its displacement does not depend on the rate at which the movements occur, but only on the geometry followed throughout the sequence. This implies that the net displacement achieved under low-*Re* conditions is independent of the duration of movements [38].
2. “Scallop theorem”: This property relies on the reversibility of a flow in a low-*Re* regime. If a moving body generates flow by reversing the same sequence, the fluid particles also follow the same trajectories; thus, the swimmer cannot achieve net displacement. This means that a reciprocal motion (symmetric sequence of movements) results in zero-net translation in every axis. Thus, a swimmer moving to a position and then returning back by reversing the same sequence of movements does not produce net displacement of the swimmer. Consequently, non-reciprocal motion has to be performed, defined by the movement of a body throughout a trajectory and returning back by implementing a different sequence of states.

2.1.2. Reciprocal and Non-Reciprocal Motion

Figure 1 illustrates the difference between reciprocal and non-reciprocal motion. The geometrical configurations acquired by the swimmer have been named with two characters corresponding to the left and right link, representing D and U when the lateral links are above or below with respect to the central link, respectively. As an example, if both links are in the upper position, the configuration is named DD; if the left link is above and the right one is below, the configuration is UD; and so on.

In the reciprocal case, the left link moves first (going from the UD configuration to DD) and the right link moves next (achieving DU configuration), returning back by the opposite sequence (the right link first and then the left link, corresponding to the sequence DD-UD). In summary, the sequence followed by the lateral links in the reciprocal case is UD-DD-DU-DD-UD, which is symmetric. In non-reciprocal motion, the return sequence differs from the reciprocal case, beginning with the left link (UU) and then rotating the right link (UD). The sequence in non-reciprocal motion is UD-DD-DU-UU-UD, where it can be seen that there is no symmetry in the sequence of movements.

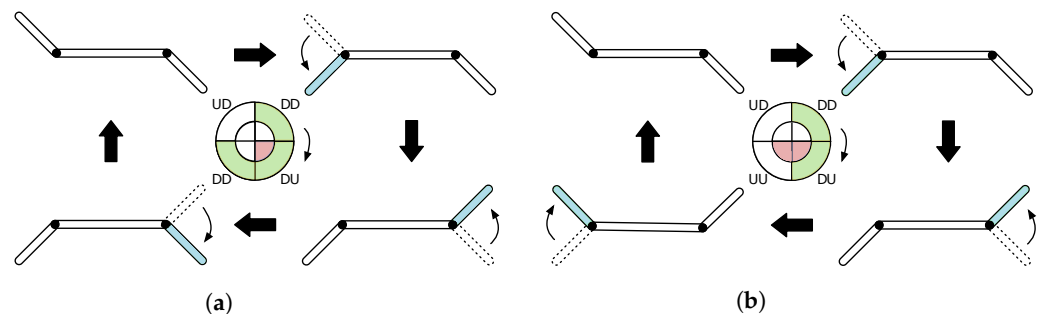


Figure 1. Types of movement: (a) reciprocal; (b) non-reciprocal. Adapted from [39].

2.2. Ideal Purcell's Swimmer

This section addresses the modelling of a Purcell's swimmer. Firstly, geometry and kinematics are introduced, followed by the description of the hydrodynamic forces that are applied to an underwater body at low- Re conditions. Consecutively, the 2D dynamic model of a Purcell's swimmer for these regimes is presented, which will be referred to as an ideal Purcell's swimmer from now on. Finally, the basics of IPMC technology and its dynamics are presented.

The theoretical model presented serves as a basis to illustrate the motion of a Purcell's swimmer. In addition, IPMC dynamics are presented to show their complexity, which is why the complete model has not been solved analytically but simulated in the MATLAB®/Simulink® environment.

2.2.1. Geometry and Kinematics

The Purcell's swimmer consists of three links connected by one degree-of-freedom (DOF) joints, as illustrated in Figure 2. The scheme shown in this figure will be taken as a reference for the kinematic and dynamic developments.

The lengths of the central and lateral links are l_0 , l_1 and l_2 , while the rotational joints are designated as j_1 and j_2 . The lateral links are supposed of equal length ($l_1 = l_2$) and the ratio $\eta = l_0/l$ relates the lengths of the links, with l being the total length of the swimmer. The ideal swimmer is composed of cylindrical links, although a different cross-section can be chosen for other designs. Regarding the angular positions of the links, θ_i represents the angular position of the i -link with respect to the X -axis of the global reference frame. The rotation of the lateral links is determined by a motion primitive or gait, which defines the angles ϕ_1 and ϕ_2 with respect to the body-fixed reference frame (x, y) . The relations between the angular position and the gait angles are $\theta_1 = \phi_1 - \theta_0$ and $\theta_2 = \phi_2 + \theta_0$. The position of the centre of i -link is defined as $\mathbf{X}_i = [x_i \ y_i \ \theta_i]^T$, with $i = \{0, 1, 2\}$, where subscript 0 refers to the central link of the Purcell's swimmer.

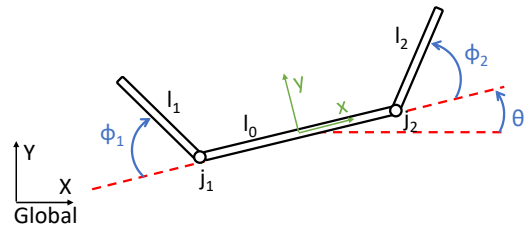


Figure 2. General scheme of Purcell's swimmer (plan view).

During the assessment of the swimmer dynamics, the movement of links l_1 and l_2 with respect to the central (or base) link is completely defined by angles ϕ_1 and ϕ_2 . On the contrary, the position of the central link is unknown.

Firstly, the position of the lateral links can be easily estimated by swimmer geometry as follows:

$$\mathbf{X}_1 = \mathbf{X}_0 + \frac{l_0}{2} \begin{bmatrix} -\cos \theta_0 \\ -\sin \theta_0 \\ 0 \end{bmatrix} + \frac{l_1}{2} \begin{bmatrix} -\cos(\phi_1 - \theta_0) \\ \sin(\phi_1 - \theta_0) \\ 0 \end{bmatrix} + \begin{bmatrix} 0 \\ 0 \\ \pi - \phi_1 \end{bmatrix} \quad (6)$$

$$\mathbf{X}_2 = \mathbf{X}_0 + \frac{l_0}{2} \begin{bmatrix} \cos \theta_0 \\ \sin \theta_0 \\ 0 \end{bmatrix} + \frac{l_2}{2} \begin{bmatrix} \cos(\phi_2 + \theta_0) \\ \sin(\phi_2 + \theta_0) \\ 0 \end{bmatrix} + \begin{bmatrix} 0 \\ 0 \\ \phi_2 \end{bmatrix} \quad (7)$$

Taking the derivatives of \mathbf{X}_1 and \mathbf{X}_2 , and writing the result in matrix form, the linear and angular velocities of the links can be expressed as [10,17,22]:

$$\dot{\mathbf{X}}_i = \mathbf{A}_i \dot{\mathbf{X}}_0 + \mathbf{B}_i \dot{\Phi} \quad (8)$$

where $\Phi = [\phi_1 \ \phi_2]^T$ and the subscript i can take values $i = \{0, 1, 2\}$, since the matrix \mathbf{A}_0 is the identity matrix and \mathbf{B}_0 is a matrix of zeros. Matrices \mathbf{A}_i and \mathbf{B}_i are defined in [17] and depend on the link whose velocity is being calculated. They are detailed in Appendix A.

2.2.2. Dynamics

The dynamics of the Purcell's swimmer depends on the forces that arise in the interaction between the swimmer and the surrounding fluid environment. In low- Re regimes, the forces opposing the swimmer motion are called drag or viscous forces, since inertial forces are neglected in these environments.

Several assumptions must be made before presenting the dynamic model [40]:

1. The robot is composed of a float ensuring that the underwater components are always placed at the same depth.
2. The fluid velocity is assumed to be zero.
3. The border effects are neglected.

The drag forces in this regime are linear as they only depend on the velocity of the swimmer. They can be obtained from the resistive force theory (RFT) by means of the following expression:

$$\begin{bmatrix} f_{v,x,i}^I \\ f_{v,y,i}^I \\ \tau_{v,i}^I \end{bmatrix} = - \begin{bmatrix} l_i \left(-c_{v,i}^\perp \sin^2 \theta_i - c_{v,i}^\parallel \cos^2 \theta_i \right) & l_i \left(c_{v,i}^\perp - c_{v,i}^\parallel \right) \cos \theta_i \sin \theta_i & 0 \\ l_i \left(c_{v,i}^\perp - c_{v,i}^\parallel \right) \cos \theta_i \sin \theta_i & l_i \left(-c_{v,i}^\perp \cos^2 \theta_i - c_{v,i}^\parallel \sin^2 \theta_i \right) & 0 \\ 0 & 0 & c_{v,i}^\circ l_i \end{bmatrix} \begin{bmatrix} \dot{x}_i \\ \dot{y}_i \\ \dot{\theta}_i \end{bmatrix} \quad (9)$$

where $f_{v,x,i}^I$, $f_{v,y,i}^I$ and $\tau_{v,i}^I$ are the drag forces and torque, $c_{v,i}^\parallel$ and $c_{v,i}^\perp$ are the tangential and normal drag coefficients, respectively, and $c_{v,i}^\circ = \frac{1}{12} c_{v,i}^\perp l_i^2$ is the drag torque parameter. The drag coefficients depend on the geometry and cross-section of the links, and they can be

calculated theoretically or through simulations. Simplifying terms and joining forces and velocities in matrices, the total drag forces and torque can be calculated as follows [10]:

$$\mathbf{F}_{v,i}^I = -\mathbf{R}_i^I \dot{\mathbf{X}}_i \quad (10)$$

where $\mathbf{F}_{v,i}^I = [f_{v,x,i}^I \quad f_{v,y,i}^I \quad \tau_{v,i}^I]^T$, and \mathbf{R}_i^I , which is called the resistance tensor, is defined by

$$\mathbf{R}_i^I = l_i \begin{bmatrix} -c_{n,i} \sin^2 \theta_i - c_{t,i} \cos^2 \theta_i & (c_{v,i}^\perp - c_{v,i}^\parallel) \cos \theta_i \sin \theta_i & 0 \\ (c_{v,i}^\perp - c_{v,i}^\parallel) \cos \theta_i \sin \theta_i & -c_{v,i}^\perp \cos^2 \theta_i - c_{v,i}^\parallel \sin^2 \theta_i & 0 \\ 0 & 0 & c_{v,i}^\circ \end{bmatrix}$$

According to a Stokes' flow, it is assumed that the swimmer is in static equilibrium and that inertial effects can be neglected. Thus, when applying Newton's second law, the components that depend on the acceleration of the swimmer can be omitted and the summation of forces must be equal to zero:

$$0 = \sum_{i=0}^2 \mathbf{F}_{v,i}^I \quad (11)$$

Substituting the expressions of $\mathbf{F}_{v,i}^I$ and $\dot{\mathbf{X}}_i$ (in which the drag forces depend) and solving for $\dot{\mathbf{X}}_0$, the velocity of the centre of the central link can be estimated as

$$\dot{\mathbf{X}}_0 = -\frac{\sum_{i=0}^2 \mathbf{R}_i^I \mathbf{B}_i}{\sum_{i=0}^2 \mathbf{R}_i^I \mathbf{A}_i} \dot{\Phi} \quad (12)$$

2.2.3. Motion Primitives

A motion primitive is a function that defines the evolution of angles ϕ_1 and ϕ_2 over time and, thus, determines the movement of links l_1 and l_2 . Motion primitives are characterised by the shape acquired when representing ϕ_2 versus ϕ_1 in the plane, which is often used to determine the name for the gait. The most common primitives are called square [5,9,10,15,22] and circular [10], as shown in Figure 3, which are applied to obtain a net displacement of the swimmer along the X-axis, as proved in other works [10,41].

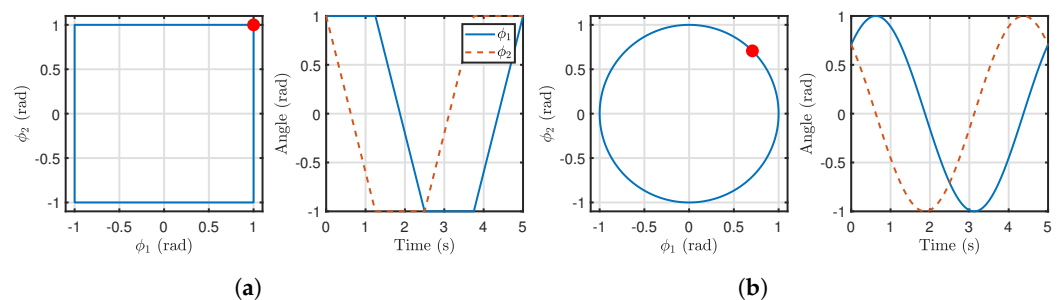


Figure 3. Most common gaits applied to the Purcell's swimmer, defined with unitary amplitude: (a) square; (b) circular. The red circular mark represents the initial point of the gait.

Based on the results of a previous work [41], the circular primitive was selected to be applied in this case. It is defined by the following expression:

$$\phi_1(t) = \epsilon \sin(2\pi f_g t + \varphi_1), \quad \phi_2(t) = \epsilon \cos(2\pi f_g t + \varphi_2) \quad (13)$$

where ϵ is the gait amplitude, f_g is the frequency, and φ_1 and φ_2 are the phase shifts of the signals.

Figure 4 illustrates the geometric configurations of the lateral segments when implementing the square gait together with the trajectory traced by the swimmer in the XY plane.

For clarity, the figure depicts only a single iteration of the gait to highlight its features. The swimmer starts at the point (0,0) (corresponding to configuration 1), moves to a higher coordinate in the Y-axis in the first part of the loop (configurations from 1 to 3), and moves backward to the initial Y-coordinate when the motion primitive finishes (configurations from 3 to 5). Although these configurations and trajectory correspond to the square gait, a similar trajectory is followed with the circular gait.

Regarding the displacement of the swimmer, it can be seen that the net displacement is achieved on the X-axis, which is consistent with the type of primitive being applied in this case (translation primitive). A slight deviation in Y can also be noticed at the end of the loop, although the displacement in X is still significantly larger. It should be remarked that the implementation of motion primitives generates upward and downward movements along the Y-axis with negligible net displacement, producing an oscillatory motion that is characteristic of motion primitive implementation.

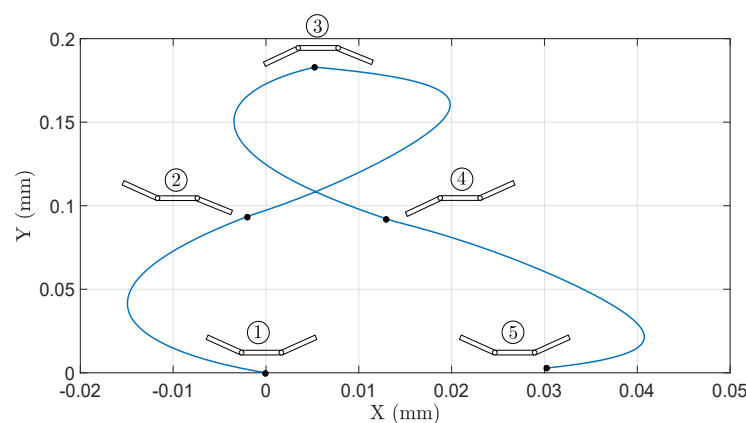


Figure 4. Trajectory followed by the centre of the central link of an ideal Purcell's swimmer during one implementation of the square gait, for $\epsilon = 1$ rad. Silicon oil was selected as fluid to achieve low- Re conditions. The geometric configurations of the lateral segments of the swimmer are indicated in the figure.

2.3. IPMC Technology

IPMC is an electroactive polymer transducer that bends upon application of voltage and generates voltage upon mechanical deformation. Its advantages include low activation voltages (4–6 V), low weight, ability to function in wet conditions, biocompatibility, simple construction, and miniaturisation [42]. This has inspired a variety of anticipated applications in robotics and biomedical engineering [43].

The IPMCs used in this study consist of a 180 μm thick NafionTM-117 membrane plated using electroless deposition with Pt electrodes, saturated with water as a solvent and ion-exchanged to the Na^+ form. Perfluorinated ionomers such as Nafion or Flemion are a typical choice for the ion-conducting polymer backbone. In addition to Na^+ and water, a variety of other cations (e.g., H^+ , Li^+ , Rb^+ , K^+ , Cs^+ , Ti^+ or Ba^+) and solvents (e.g., ethylene glycol or glycerol) or ionic liquids (e.g., TBA^+ and TMA^+) can be used in Nafion [44].

IPMC actuation is based on the physical transport of ion species. Applying a voltage between the IPMC electrodes creates an electric field across the membrane. The mobile counterions (Na^+) are weakly coupled to the polymer backbone (Nafion) and migrate in the presence of the electric field. The hydrated counterions carry the solvent molecules (water) with them, causing an uneven distribution of charge and mass across the membrane (see Figure 5). The electrostatic and hydrostatic forces between the mobile counterions, the solvent and the polymer backbone cause a bending moment in the IPMC.

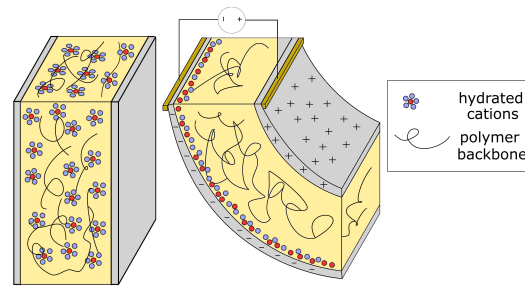


Figure 5. Ion motion when a potential difference is applied. Internal forces are generated inside the polymer, forcing the bending. Image reproduced from [44].

The dynamics of IPMCs for actuation can be described by partial differential equations for charge (from the Poisson–Nernst–Planck equation) and bending dynamics (from Euler–Bernoulli beam theory). Several complex models can be found in the literature combining the mechanical dynamics of the flexible beam and the electrical dynamics [44–46]; they are not presented here due to their complexity.

3. Methodology

This section deals with the methodology followed to investigate the effect of the flexibility of IPMC joints of a Purcell’s three-link swimmer on its locomotion. Firstly, details of the prototype design and equipment are given. Then, the robot simulation model is described. Finally, details of the testing procedures are explained, including considerations of the fluid environments and data processing to estimate swimmer displacement.

3.1. Purcell’s Swimmer Prototype

As illustrated in Figure 6, the IPMC-based Purcell’s swimmer prototype is composed of two distinct components: a submerged structure and a float. The former consists of three links of rectangular cross-section that comprise the swimmer. Each of these links is constructed from two pieces, which include slits that permit the attachment of both the IPMCs and the gold electrodes necessary for their power supply to the links with no slack by pressure, assembled in a sandwich configuration. In order to guarantee that the swimmer remains afloat, a piece of plastic is positioned on the upper surface of the central link.

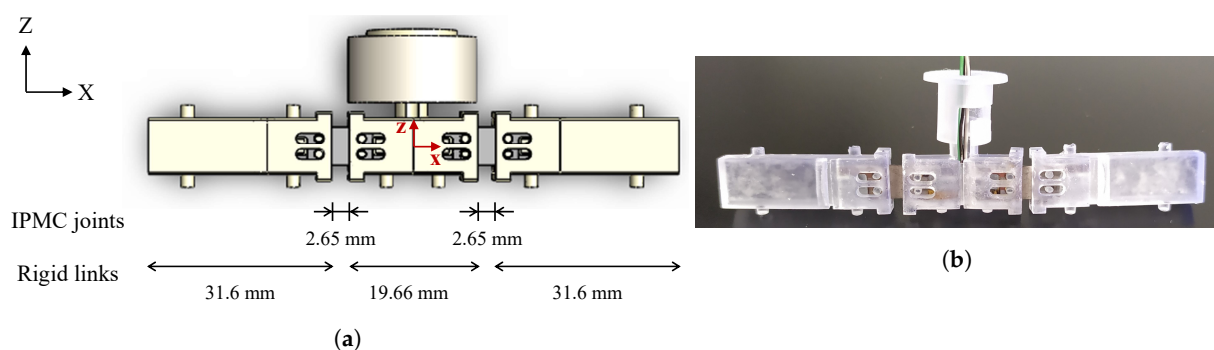


Figure 6. Front view of the Purcell’s swimmer IPMC-based prototype: (a) design in SolidWorks; (b) fabricated prototype. Note that the reference frame of these images is different from that of Figure 2.

The length of the links was determined based on the findings of our previous study reported in [41], which established the ratio $\eta = 0.223$ for the maximum displacement for the classical circular primitive. Thus, by selecting $l_0 = 19.66$ mm to adequately accommodate IPMCs and their electrodes, the total length of the swimmer was obtained as

$$l = \frac{l_0}{\eta} = 88.16 \text{ mm}$$

Considering lateral links of equal length, the length of each of them was obtained by taking into account the length of each actuator (i.e., 2.65 mm) as follows:

$$l = l_0 + l_1 + l_2 + 2l_{IPMC} \xrightarrow{l_1=l_2} l = l_0 + 2l_1 + 2l_{IPMC} \quad (14)$$

$$l_1 = \frac{l - l_0 - 2l_{IPMC}}{2} = 31.6 \text{ mm}$$

The swimmer dimensions are also summarised in Table 2.

With regard to the fabrication of the prototype, the mechanical parts were produced via stereolithography, utilising the Envisiontec Micro Plus Hi-Res 3D printer with 3DM-tough resin (from ADMAT Inc., Richwiller, France) [47]. Subsequently, the parts were cleaned using ultrasound and cured by heat and ultraviolet light. The fabrication of the IPMC sheets was conducted in accordance with the procedure described in [48,49]. The IPMCs and the gold electrodes were cut using a micro laser etching machine, the Optec WS Starter (Spectra Physics Talon 355-15 source, from MKS Instruments Inc., Andover, MA, USA). The finished actuator samples were then subjected to cleaning and a protonation process, which involved maintaining them in a 0.1 M HCl solution for a minimum of 24 h and subsequently undergoing an ion exchange into Na⁺ form in a 0.1 M NaOH solution for a similar period. Finally, the samples were rinsed in deionised water prior to use.

Table 2. Dimensions of the IPMC-based prototype. The lateral links are considered to be of equal length.

Value of η	Length of Central Segment (mm)	Length of Lateral Segments (mm)	Total Length of the Swimmer (mm)
0.2230	19.66	31.6	88.16

3.2. Equipments

The setup used for the experiments is illustrated in Figure 7 and consists of

- A tank with fluid where the swimmer, shown in Figure 7a, is floating. Considering the small dimensions of the prototype, a small tank similar to an aquarium in dimensions was selected, as shown in Figure 7b. To ensure a low Re , two different fluids were tested with different densities and viscosities: water mixed with glycerine (in order to decrease the characteristic Re of the water), and water mixed with dishwashing detergent (as the generated bubbles decrease the inertial effects).
- A computer (Figure 7c), in which a LabVIEW program (from National Instruments Inc., Austin, TX, USA) runs to send the excitation signals (namely the clockwise circular gait defined by Equation (13)) to the IPMCs as

$$\begin{aligned} v_1(t) &= A \sin(2\pi f_g t + \varphi_1) \\ v_2(t) &= A \cos(2\pi f_g t + \varphi_2) \end{aligned} \quad (15)$$

where A is the amplitude in V, f_g is the frequency in Hz, φ_i is the phase shift in radians, and v_1 and v_2 are the voltage signals applied to the left and right IPMCs, respectively.

- A USB data acquisition board from National Instruments (NI-USB6009) and a custom-built buffer amplifier (based on the LM675T operational amplifier from Texas Instruments Inc., Dallas, TX, USA) were used to ensure an adequate power supply to IPMCs (see Figure 7c). As can be observed in Figure 7b, the IPMCs were powered by long and flexible cables, which were attached at a height above the tank to minimise their impact on the swimmer's movement.
- A zenithal-view external camera was used to record the displacement of the swimmer during the experiments with a velocity of 30 frames per second.

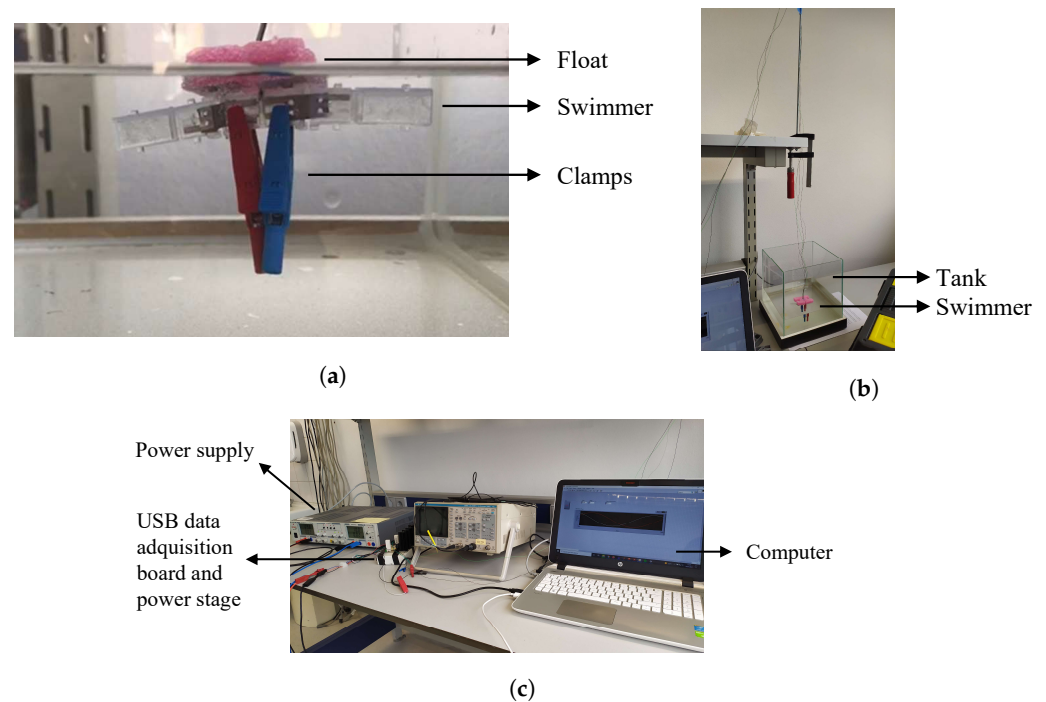


Figure 7. Setup used for the IPMC-based prototype experiments: (a) swimmer (float in pink colour, and clamps to apply pressure on the IPMCs in red and blue colours); (b) tank with the swimmer; (c) PC, power supply, USB data acquisition board, and power stage.

3.3. Simulation Model

The construction of an analytical model for the IPMC-based Purcell’s swimmer is a challenging undertaking, mainly due to the complexity of modelling IPMC dynamics and its integration into the ideal model described in Section 2.2. Note that IPMC dynamics would have an effect on the gait angles ϕ_1 and ϕ_2 , so they should be included in both the swimmer kinematics and dynamics. Instead, a simulation model was built using the Simscape™ toolbox of the MATLAB®/Simulink® software (from The MathWorks Inc., Natick, MA, USA) in its R2022b version. This toolbox allows us to compute the displacement of the swimmer based on its physical components and the environment conditions, as opposed to solving the analytical dynamic model. Furthermore, a Simulink model will allow us to be able to perform closed-loop simulations in future.

The general scheme of the simulation model developed is shown in Figure 8. It consists of different subsystems (from top to bottom in the above figure): the excitation signals sent to the IPMCs (i.e., voltages of the form of Equation (15)), the Purcell’s swimmer itself, the environment configuration, and drag (viscous) forces applied to each swimmer segment. The remaining subsystems of the scheme are described below.

The links of the Purcell’s swimmer were modelled as rigid blocks. For illustration purposes, the models of the right and central segments are shown in Figure 9a and 9b, respectively, where it can be observed that the rigid links were modelled by the “Solid” block. Moreover, to allow for the movement of the swimmer in the XY plane, a planar joint was added between the central segment and the world reference frame by means of the “Planar joint” block (see Figure 9b).

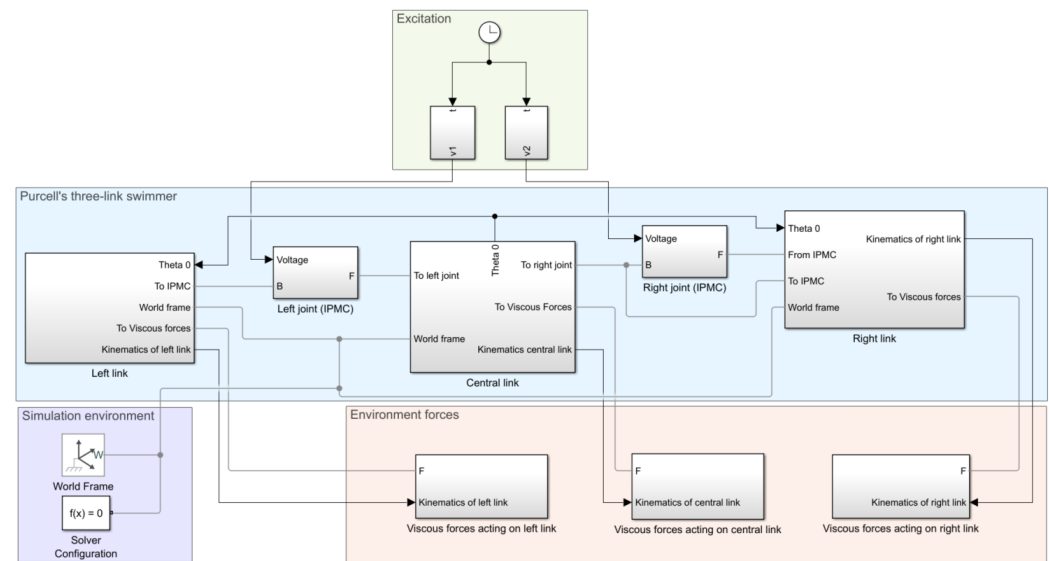


Figure 8. MATLAB®/Simulink® main scheme developed to simulate the IPMC-based Purcell's swimmer prototype.

Regarding the IPMCs, their deformation can be described by a physical-based model that incorporates both their mechanical and electrochemical properties, as outlined in [46]. The mechanical behaviour was modelled as flexible beams simulating its bending, as illustrated in Figure 9c. Each flexible beam is composed of a set of elements (ten, in this case) that are repeated and connected in series, where each of them, in turn, is made up of two rigid elements coupled by “Revolute joint” blocks (see Figure 9d). These joints provide the flexibility inherent to IPMCs, and they were configured with a spring stiffness and a damping coefficient obtained from the identification carried out for an IPMC-based three-link swimmer in [30]. To simplify electrochemistry behaviour, a torque output depending of the voltage input, represented by a first-order transfer function (the parameters of which depend on the specific IPMCs [50]), was sent to the revolute joints of each actuator, as can be seen at the top of Figure 9c. These flexible elements account for the distributed parameter part dynamics from torque to tip deflection.

With respect to the fluid environment, Simulink® does not allow us to simulate the hydrodynamics of a specific environment, so it was necessary to add constraints that mimic the effects of drag forces in the fluid (calculating them theoretically). In low- Re regimes, only viscous forces appear in the environment, which can be calculated via RFT, as detailed in Section 2.2.2. The constrictions were added using the block called “External Force and Torque”, as shown in Figure 9e, being applied to the centre of mass of each segment of the swimmer. The forces were applied to the X- and Z-axes of Simulink® because these correspond to the longitudinal and normal axes of the swimmer, while the torque was applied to the Y-axis. The values of the drag coefficients were estimated through COMSOL Multiphysics®, as detailed in [51].

Finally, additional blocks pertaining to the simulation environment, including “World Frame” and “Solver Configuration”, were incorporated into the model to establish the reference coordinate system and define solver settings for simulation, respectively (see bottom-left side of Figure 8).

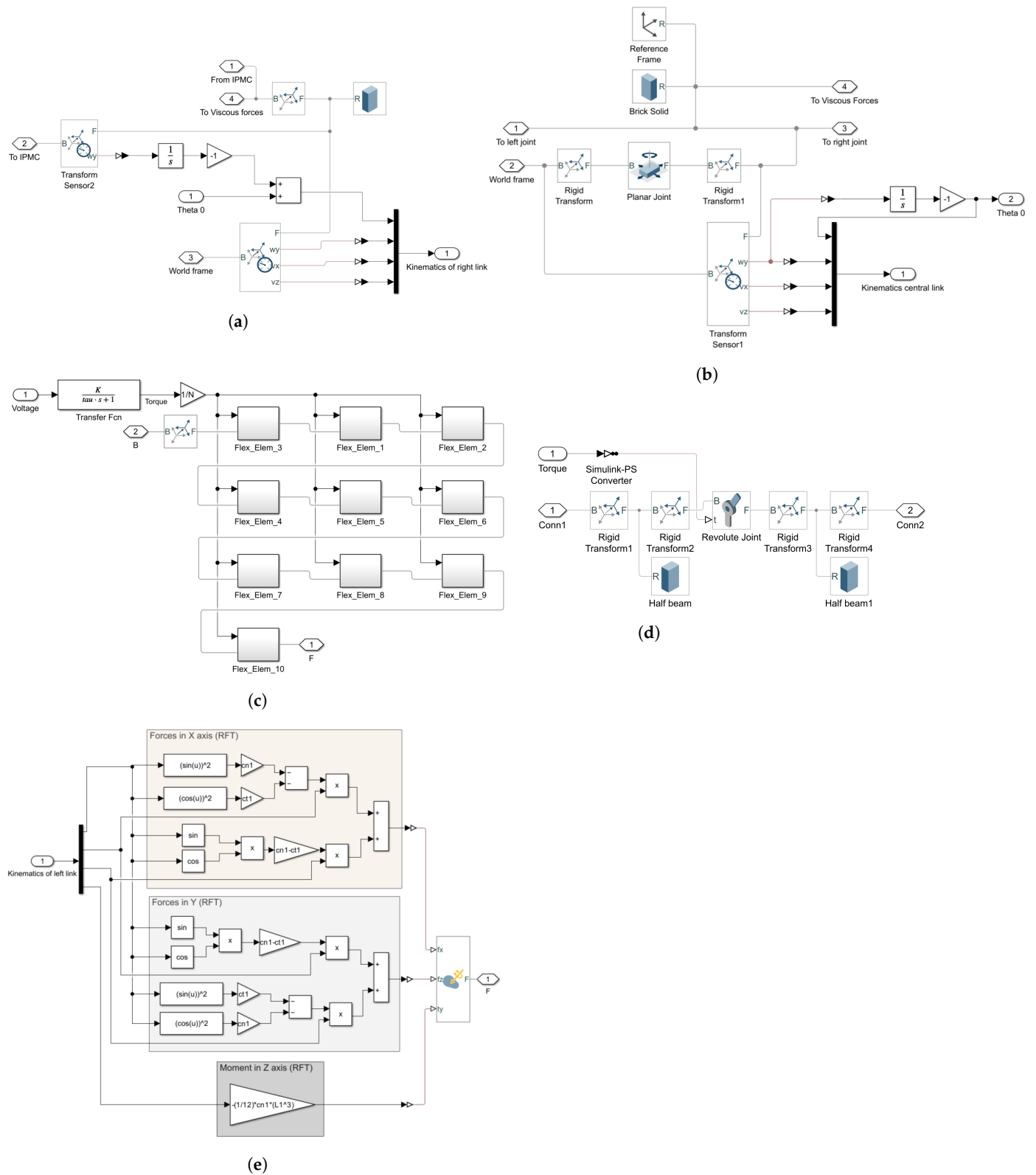


Figure 9. Simulink® scheme used for modelling of the IPMC-based Purcell's swimmer: (a) right link; (b) central link; (c) IPMC actuator model; (d) detail of a flexible element of each IPMC actuator; (e) linear drag forces of the environment.

3.4. Testing Procedures

Both simulations and experiments were performed in an open loop scheme, applying the circular primitive continuously for different excitation voltages, frequencies, and phase

shifts to the IPMCs in order to evaluate its influence on the swimmer displacement. In particular, the excitation parameters considered were as follows: 4 V of amplitude, a frequency of 1.5 Hz, and a phase shift of 1.5 rad for simulations; and 3–4 V, 1–1.5 Hz, and 1.5–2.35 rad for experiments.

In light of their significance, some considerations of both the fluid environments and the data processing to estimate the swimmer displacement are detailed next.

3.4.1. Fluid Environments

The hypothesis of a low Re is proposed as a starting point for this work. In consideration of the dimensions of the robot, this value was deliberately reduced by increasing the viscosity of the fluid in which the robot navigates. In particular, two mixtures with a volume fraction of 50:50 were considered as fluids: one comprising water and glycerine, and the other comprising water and dishwashing detergent.

The density and viscosity of a homogeneous mixture can be calculated by averaging the respective parameters. The mixture of water and glycerine produces a fluid with a density of 1130 kg/m³ and viscosity of 0.7455 kg/(m·s), while the mixture of water and dishwashing detergent produces a fluid with a density of 1016.55 kg/m³ and viscosity of 0.5 kg/(m·s) (see Table 3). In terms of swimming performance, this is equivalent to a reduction in the size of the Purcell’s swimmer by a factor of approximately 650, which is a common method used in the experimental evaluation of marine vessels and aircraft.

Specifically, a total of four experiments were performed with these mixtures: one with water mixed with glycerine and three with water mixed with dishwashing detergent. Concerning simulations, they were carried out in a water-glycerine bath. This initial low- Re hypothesis will be confirmed for both simulations and experiments in Section 4 by calculating the value of Re from the measured velocity of the swimmer, its total length, and the properties of the fluids under consideration.

Table 3. Fluids used to prepare mixtures for experiments with the IPMC-based prototype.

Fluid	Density (kg/m ³)	Viscosity (kg/(m·s))
Water	1000	1.002×10^{-3}
Glycerine	1260	1.49
Dishwashing detergent	1033.1	1
50:50 volume fraction mixtures	Density (kg/m ³)	Viscosity (kg/(m·s))
Water + Glycerine	1130	0.7455
Water + Dishwashing detergent	1016.55	0.5

3.4.2. Linear Displacement Tracking

The primary objective of both simulations and experiments was to measure the linear displacement of the central segment of the swimmer. In the simulations, this was achieved by tracking a virtual sensor placed at the centre of the central link. For the experiments, the displacement was determined by analysing video recordings of the swimmer motion.

To identify the trajectory followed by the prototype during the experiments, the speeded-up robust features (SURF) algorithm [52] in MATLAB® was used to find blob features. First, the video frames were rotated to align the X- and Y-axes of the images and the swimmer to correctly calculate the displacement in both axes. The video was then processed frame by frame to generate binary images, filtering out non-marker objects to improve the detection accuracy. Subsequently, objects that differed from the marker size were excluded and the SURF algorithm was applied.

Concerning the duration of simulations and experiments, it should be remarked that there was a significant disparity: while experiments were conducted for approximately 20 min, simulations were limited to one minute due to computational constraints. Due to this fact, to enable a fair comparison, the displacement of the swimmer from both simulations and experiments was normalised to a per-minute basis. In particular, the

average velocity in the X-direction was calculated by dividing the total displacement by the experiment duration. For simulations, this normalised displacement corresponded to the value at the end of the one-minute simulation.

4. Results

This section presents the results of simulations and experiments conducted on the IPMC-based Purcell's swimmer prototype, followed by a comparative discussion.

4.1. Simulation Results

The simulated displacements of the swimmer in the X- and Y-directions were obtained and are plotted in Figure 10. For the excitation frequency of 1.5 Hz, the swimmer executed 90 motion primitives over the 60 s experiment duration, attaining a net X-displacement of 0.2149 mm and a corresponding velocity of 0.2149 mm/min.

It is observed that the net displacement was achieved along the X-axis, similarly to the ideal Purcell's swimmer studied in Section 2.2.3. Both the X- and Y-displacements are characterised by oscillatory motions, although the X-displacement can be approximated to a straight line due to its small amplitude (2.78×10^{-4} mm with net displacement 2.3×10^{-3} mm/cycle), as seen at the top of Figure 10.

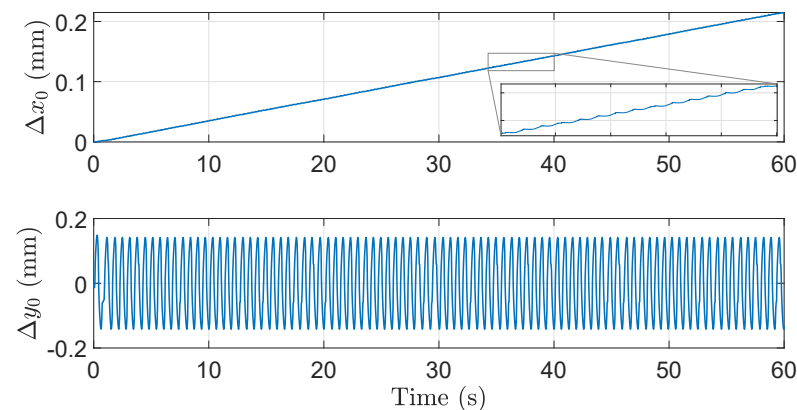


Figure 10. Simulated displacement of the centre of the central link of the IPMC-based Purcell's swimmer in water mixed with glycerine environment, for a total simulation time of $T_f = 1$ min.

Concerning lateral motion along the Y-axis, the upward and downward movements, typical of the motion primitives and observed in the ideal scenario, are evident in this particular case. These oscillations had an amplitude of 0.15 mm, consistent with the dimensions of the swimmer. While a slight drift was detected between the initial and final oscillations, it was too small to be visually apparent in the figure. This drift, approximately -3.7×10^{-5} mm, indicates a gradual deviation in the oscillations from the X-axis toward the negative Y-direction. Although this drift is typical of motion primitives and accumulates over time, its impact was minimal in this case due to the small amplitude and relatively short simulation duration. These observations are in agreement with the motion primitive analysis presented in Section 2.2.3.

To validate the initial hypothesis of a low- Re environment, this dimensionless number is estimated based on the velocity obtained (0.2149 mm/min), the total length of the swimmer (88.16 mm), and the characteristics of the mixture of water and glycerine detailed in Table 3. This results in $Re = 4.78 \times 10^{-4}$, which is below 1 and validates the assumption of a low- Re regime.

4.2. Experimental Results

Table 4 provides a summary of the excitation parameters and corresponding experimental results. For each experiment, the final displacement of the swimmer, in mm, and the normalised displacement, in mm/min, were calculated. These results show that the

swimmer moved the most in the water-glycerine bath, followed by the final experiment with water and the dishwashing detergent. Both experiments used similar parameters for the primitive, specifically 1.5 Hz and 4 V, differing only in the phase shift of the sinusoidal signals. The third highest displacement was obtained in the experiment with water and dishwashing detergent at 1 Hz and 3 V, while the least displacement was observed in the case with excitation at 1 Hz and 4 V.

Table 4. Results of displacement at the centre of the central link of the IPMC-based prototype during experiments.

Fluid	Excitation Signal			Δx_0 (mm)	Δx_0 (mm/min)	Re ($\times 10^{-4}$)
	Frequency f_g (Hz)	Voltage A (V)	Phase Shift φ_i (rad)			
Water + glycerine	1.5	4	1.508	4.94	0.2148	4.78
Water + detergent	1	3	$\pi/2$	2.45	0.1114	3.33
Water + detergent	1	4	$\pi/2$	1.368	0.0636	1.90
Water + detergent	1.5	4	$3\pi/4$	3.75	0.1786	5.34

According to the results, a relationship was found between the frequency and amplitude of the sinusoidal power signals of the IPMCs, since the best results were obtained by increasing both parameters simultaneously, compared to increments in only one. Furthermore, a conclusion can be drawn regarding the optimal gait parameters: the swimmer achieves higher displacement when the IPMCs are excited at 1.5 Hz and 4 V.

To validate the assumption of low- Re number conditions, Re was calculated for the experiments listed in Table 4, using the velocity of the swimmer calculated for each of them. It can be confirmed that, for all experiments, Re is clearly below 1, indicating that the dominantly Stokes swimming regime assumption was appropriate.

The swimmer positions at different times during the experiments are shown in Figure 11 for the experiment with water mixed with glycerine (1.5 Hz and 4 V). Three positions of the swimmer movement during the experiment can be seen in Figure 11a–c, while Figure 11d is the superposition of the previous images of the swimmer during the experiment. This last figure shows minor differences between the initial and final positions of the swimmer, although it is clear that it only moved a few millimetres.

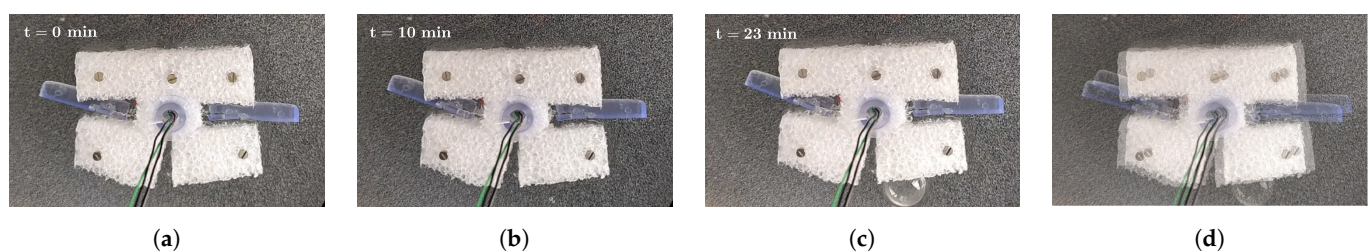


Figure 11. Positions of the IPMC-based prototype at different instants of the experiment with water-glycerine mixture: (a) at the beginning; (b) halfway through; (c) at the end; (d) overlap of start and end positions.

Figure 12 shows the displacement of the prototype during one minute of the experiment with a water-glycerine mixture, together with the displacement obtained in the simulation (the whole simulation). It should be noted that these results correspond to a single minute of the experiment; therefore, their values may not exactly match those presented in Table 4. This is because the prototype was constantly moving forward and backward on both axes, so it is likely that the displacement was different at different times of the experiment. Therefore, the displacement of an isolated minute of the experiment differs from the average displacement calculated in Table 4. In addition, the same figure shows occasional deviations that may be due to a software detection error. They may also affect the differences between the one-minute and overall results.

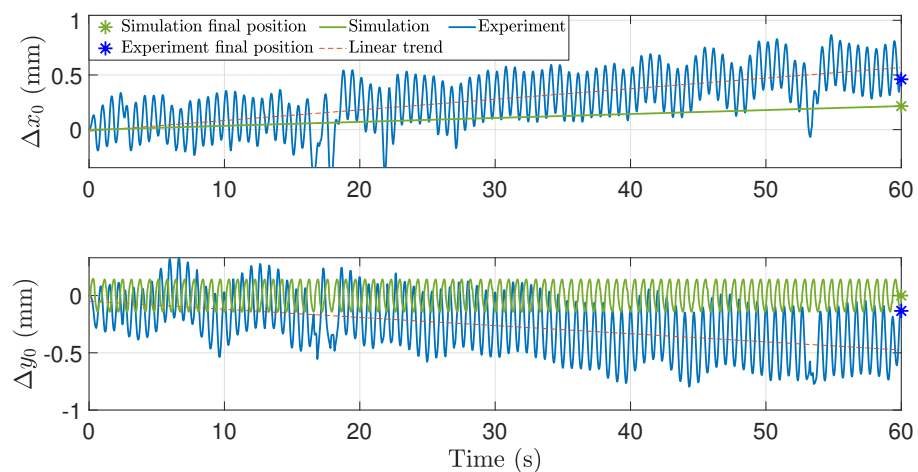


Figure 12. Displacement of the IPMC-based Purcell’s swimmer prototype in the water-glycerine mixture, during the first minute of both the simulation and the experiment. Linear trend refers to experiments; notice that it does not correspond to the final displacement of the swimmer.

Figure 12 also illustrates that the swimmer exhibits movement in both the X- and Y-directions. However, the net displacement regarding the X-axis is greater than that achieved in the Y-axis: 0.4603 mm in the X-axis versus -0.134 mm in the Y-axis for the first minute. Both displacements were approximated by a line (in red) to facilitate an appreciation of the trend in the robot movement. Furthermore, upward and downward movements are observed, occurring along both axes, with amplitudes of approximately 0.2 mm in the X-axis and 0.3 mm in the Y-axis. While the drift in the Y-direction occurs in all cases and accumulates over time, increasing the swimmer deviation, it is almost unnoticeable in simulations. It is also noteworthy that the number of primitives implemented in this figure is between 88 and 90, which corresponds to the excitation frequency of the IPMCs and, therefore, to the frequency of the motion primitive (1.5 Hz).

4.3. Discussion

To facilitate the comparison between simulation and experimental results, key numerical findings are summarised in Table 5. Both simulation and experimental data indicate that the swimmer moves in the positive X-direction and the negative Y-direction. The negative Y-drift in simulations was calculated in Section 4.1, although it is not visually apparent in the results plotted in Figure 12, where, in contrast, the experimental data clearly exhibit this drift. Swimmer movement magnitudes and displacements aligned with prototype dimensions, resulting in identical normalised displacement per minute for both simulations and experiments. Furthermore, both scenarios executed nearly the same number of primitives per minute (about 90 repetitions), matching the IPMC excitation and motion primitive frequency of 1.5 Hz.

Figure 12 illustrates similar X-axis displacement directions and magnitudes in simulations and experiments, with movement toward the positive X-axis. Both exhibit upward and downward motion along Y-axis. However, experiments reveal X-axis oscillations of the swimmer, indicating continuous back-and-forth movement, unlike the more linear X-axis trajectory obtained in simulations. As summarised in Table 5, simulation amplitudes are lower, especially on the X-axis, while Y-amplitudes are doubled in the experiments compared to the simulations. Despite these differences, the overall magnitudes remain consistent with the prototype dimensions.

Regarding the differences between the simulation and the experiments, it should be noted that, as mentioned above, Figure 12 shows the results of a single minute of an experiment. Since the displacement of the robot varies during the experiments, the displacement obtained in this precise minute may not coincide with the normalised one

calculated from the total displacement and, therefore, with the one obtained in simulations. Despite this, the main differences are found in the magnitude of the oscillations along the X-axis. It is important to note that, while the simulation environment aimed for low- Re conditions, inertial forces were not entirely negligible due to the inherent density of the rigid links and IPMCs. Although these environmental forces were not modelled in Simulink®, there is a high probability that the inertia of the swimmer still influenced its behaviour to some extent. It may thus be reasonably concluded that neither the simulations nor the experiments perfectly represented pure low- Re conditions. In fact, if Re was calculated based on a velocity other than that of the centre of the swimmer, such as the linear velocity of the lateral links tip, Re would be closer to one and, therefore, the inertial forces could not be completely neglected.

Table 5. Comparison between simulation and experimental results.

	Direction of Movement	X-Normalised Displacement (mm/min)	Number of Gaits in 1 min	X-Amplitude (mm)	Y-Amplitude (mm)
Simulations	+X, −Y	0.2149	90	2.78×10^{-4}	0.15
Experiments	+X, −Y	0.2148	88–90	0.2	0.3

Furthermore, with respect to the fluid environment, it was necessary to model it using the viscous forces determined by RFT, as it was not possible to simulate a fluid environment in MATLAB®/Simulink®. Regarding these viscous forces, the drag coefficients were calculated on the assumption that the fluid mixtures were homogeneous mixtures whose density and viscosity could be determined. However, these mixtures may not have been homogeneous in the experiments; therefore, the magnitude of these forces in the simulations may not be comparable to those in the experiments. This would affect the displacement of the swimmer, as viscous forces oppose the direction of movement.

Another discrepancy between simulations and experiments stems from the absence of a float in the model, which could have influenced the fluid–swimmer interaction and surface friction. Additionally, the experimental setup involved thin, flexible cables to power the IPMCs, which may have unintentionally affected swimmer movement. These cables could have acted as anchor points, restricting the freedom of motion and potentially altering swimmer performance.

Despite the above and following the results presented, it has been demonstrated that the prototype was able to move successfully within the specified environments, thereby validating both the model and the subsequent design. However, several experimental limitations were encountered. Among these, accurate trajectory recording proved to be challenging due to the combination of low video resolution and the small amplitude of prototype movements.

Moreover, IPMC technology is suitable for these applications as it offers significant advantages for microrobotics. However, practical considerations are essential. Prior activation in HCl and NaOH solutions and the material's inherent low torque, limiting object manipulation capabilities, are notable challenges. Consequently, the lateral links of the swimmer exhibited restricted amplitude during experiments, leading to minimal displacement of the prototype. In addition, the gold electrodes were covered with oxidation residues upon contact with the fluid, potentially leading to elevated contact resistances and consequently reduced torque generation by the IPMC, affecting the overall results. The characteristics and cares of IPMCs must be taken into account when incorporating them into these types of robots.

5. Conclusions

This paper has presented a few-centimetre prototype of Purcell's swimmer designed to navigate in low-Reynolds-number (Re) regimes, with joints made of ionic polymer–metal composite (IPMC) sheets that bend when a voltage is applied, thus allowing the lateral links to rotate. The theoretical modelling of the ideal Purcell's swimmer was developed,

followed by the description of the fabricated prototype, the simulations and experiments carried out, together with the discussion of the results obtained.

The simulations were performed in the software MATLAB®/Simulink® by means of the physical modelling tool Simscape™, and the results demonstrated that the swimmer could move under low-*Re* conditions. Net displacement was achieved along the X-axis, with a small drift in the Y-direction, negligible compared to the X-displacement. Upward and downward movements along the Y-axis are observed, typical of motion primitive implementation.

In experiments, two different fluids with different densities and viscosities were tested: water mixed with glycerine and water mixed with a dishwashing detergent. The best results were achieved with water and glycerine. The conclusion of these experiments is that the swimmer was able to operate in low-*Re* conditions, but with several limitations, mainly derived by IPMCs. Nevertheless, the successful navigation of the prototype within these environments validates both the model and its subsequent design.

Comparison of simulation and experimental results reveals both resemblances and discrepancies. Both scenarios demonstrate consistent swimmer direction and net X-displacement. The amplitudes of upward and downward movements in the X- and Y-directions are similar and consistent with the prototype dimensions. Moreover, the number of motion primitives executed per minute aligns in both cases, consistent with the IPMC excitation frequency and gait period.

The IPMC actuator was found to exhibit both advantages and disadvantages, with a number of areas for potential improvement identified. Its advantages include low applied voltage (4–6 V), low density, and potential biocompatibility and biodegradability. However, its disadvantages suggest that it may not be ideal for this type of prototype, as it degrades over time, and maintaining its performance under bending is challenging. Research into alternative materials that are similar to IPMCs, but with less degradation over time, could be beneficial as this would improve the usability of both the materials and the robot.

Besides the actuation material challenges, future research should address enhancing the experimental conditions. This concerns employing a homogeneous fluid to facilitate the attainment of low-*Re* conditions, eliminating the need for fluid mixing. Furthermore, granting the prototype greater autonomy by reducing cable forces would significantly improve manoeuvrability. Finally, Simulink simulations would allow us to test possible closed-loop strategies that can later be applied to the prototype.

Author Contributions: Conceptualization, I.T. and B.M.V.; methodology, C.N.-G., I.T. and B.M.V.; software, C.N.-G.; validation, C.N.-G.; formal analysis, C.N.-G.; investigation, C.N.-G. and A.H.; resources, I.T., A.H. and B.M.V.; data curation, C.N.-G.; writing—original draft preparation, C.N.-G. and I.T.; writing—review and editing, C.N.-G., I.T., A.H. and B.M.V.; visualization, C.N.-G.; supervision, I.T. and B.M.V.; project administration, I.T. and B.M.V.; funding acquisition, I.T. and B.M.V. All authors have read and agreed to the published version of the manuscript.

Funding: This work was partially supported by the Consejería de Economía e Infraestructuras (Junta de Extremadura) through the grants “Ayuda a Grupos de Investigación de Extremadura” no. GR21168 and GR18159 and the project IB18109, and partially by the European Regional Development Fund “A way to make Europe”. Cristina Nuevo-Gallardo would like to thank Universidad de Extremadura for its support through the scholarships “Plan de Iniciación a la Investigación, Desarrollo Tecnológico e Innovación” in the 2018 and 2019 editions.

Institutional Review Board Statement: Not applicable.

Informed Consent Statement: Not applicable.

Data Availability Statement: The data will be available under request.

Acknowledgments: Special thanks to Delft University of Technology (TU) for providing the materials and equipment for the fabrication and development of the experiments with the designed prototype.

Conflicts of Interest: The authors declare no conflicts of interest.

Abbreviations

The following abbreviations are used in this manuscript:

Re	Reynolds number
IPMC	Ionic polymer–metal composite
RFT	Resistive force theory
SURF	Speeded-up robust features

Appendix A. Kinematic Variables

This appendix develops the expressions for the velocity of the i -link, as well as the variables that define these expressions for the central, left and right segments.

Regarding the linear and angular velocities of the links, they can be expressed as [10,17,22]:

$$\dot{\mathbf{X}}_i = \mathbf{A}_i \dot{\mathbf{X}}_0 + \mathbf{B}_i \dot{\Phi} \quad (\text{A1})$$

where matrices \mathbf{A}_i and \mathbf{B}_i are defined in [17] as follows:

- Central link: $\mathbf{A}_0 = \mathbf{I}_3$ and $\mathbf{B}_0 = 0_{3 \times 2}$
- Left link:

$$\mathbf{A}_1 = \begin{bmatrix} 1 & 0 & \frac{l_0}{2} \sin \theta_0 - \frac{l_1}{2} \sin(\phi_1 - \theta_0) \\ 0 & 1 & -\frac{l_0}{2} \cos \theta_0 - \frac{l_1}{2} \cos(\phi_1 - \theta_0) \\ 0 & 0 & 1 \end{bmatrix}; \quad \mathbf{B}_1 = \begin{bmatrix} \frac{l_1}{2} \sin(\phi_1 - \theta_0) & 0 \\ \frac{l_1}{2} \cos(\phi_1 - \theta_0) & 0 \\ -1 & 0 \end{bmatrix}$$

- Right link:

$$\mathbf{A}_2 = \begin{bmatrix} 1 & 0 & -\frac{l_0}{2} \sin \theta_0 - \frac{l_2}{2} \sin(\phi_2 + \theta_0) \\ 0 & 1 & \frac{l_0}{2} \cos \theta_0 + \frac{l_2}{2} \cos(\phi_2 + \theta_0) \\ 0 & 0 & 1 \end{bmatrix}; \quad \mathbf{B}_2 = \begin{bmatrix} 0 & -\frac{l_2}{2} \sin(\phi_2 + \theta_0) \\ 0 & \frac{l_2}{2} \cos(\phi_2 + \theta_0) \\ 0 & 1 \end{bmatrix}$$

References

1. Moshayedi, A.J.; Khan, A.S.; Davari, M.; Mokhtari, T.; Emadi Andani, M. Microrobots for the Healthcare System from Design to Application – State of the Art and Challenges. *EAI Endorsed Trans. AI Robot.* **2024**, *3*, 1–16.
2. Lee, J.G.; Raj, R.R.; Day, N.B.; Shields, C.W.I. Microrobots for Biomedicine: Unsolved Challenges and Opportunities for Translation. *ACS Nano* **2023**, *17*, 14196–14204. [[CrossRef](#)] [[PubMed](#)]
3. Purcell, E.M. Life at low Reynolds number. *Am. J. Phys.* **1977**, *45*, 3–11. [[CrossRef](#)]
4. Becker, L.E.; Koehler, S.A.; Stone, H.A. On self-propulsion of micro-machines at low Reynolds number: Purcell’s three-link swimmer. *J. Fluid Mech.* **2003**, *490*, 15–35. [[CrossRef](#)]
5. Tam, D.; Hosoi, A.E. Optimal stroke patterns for Purcell’s three-link swimmer. *Phys. Rev. Lett.* **2007**, *98*, 068105. [[CrossRef](#)] [[PubMed](#)]
6. Avron, J.E.; Raz, O. A geometric theory of swimming: Purcell’s swimmer and its symmetrized cousin. *New J. Phys.* **2008**, *10*, 063016. [[CrossRef](#)]
7. Or, Y. Asymmetry and Stability of Shape Kinematics in Microswimmers’ Motion. *Phys. Rev. Lett.* **2012**, *108*, 258101. [[CrossRef](#)]
8. Hatton, R.L.; Choset, H. Geometric Swimming at Low and High Reynolds Numbers. *IEEE Trans. Robot.* **2013**, *29*, 615–624. [[CrossRef](#)]
9. Alouges, F.; DeSimone, A.; Giraldo, L.; Zoppello, M. Self-propulsion of slender micro-swimmers by curvature control: N-link swimmers. *Int. J. Non-Linear Mech.* **2013**, *56*, 132–141. [[CrossRef](#)]
10. Wiesel, O.; Or, Y. Optimization and small-amplitude analysis of Purcell’s three-link microswimmer model. *Proc. R. Soc. A Math. Phys. Eng. Sci.* **2016**, *472*, 4–25. [[CrossRef](#)]
11. Kadam, S.; Phogat, K.S.; Banavar, R.N.; Chatterjee, D. Exact Isoholonomic Motion of the Planar Purcell’s Swimmer. *IEEE Trans. Autom. Control.* **2022**, *67*, 429–435. [[CrossRef](#)]
12. Kadam, S.; Banavar, R. Geometry of locomotion of the generalized Purcell’s swimmer: Modelling, controllability and motion primitives. *IFAC J. Syst. Control.* **2018**, *4*, 7–16. [[CrossRef](#)]
13. Grover, J.; Zimmer, J.; Dear, T.; Travers, M.; Choset, H.; Kelly, S.D. Geometric Motion Planning for a Three-Link Swimmer in a Three-Dimensional low Reynolds-Number Regime. In Proceedings of the 2018 Annual American Control Conference (ACC), Milwaukee, WI, USA, 27–29 June 2018; pp. 6067–6074.

14. Kadam, S.; Joshi, K.; Gupta, N.; Katdare, P.; Banavar, R.N. Trajectory tracking using motion primitives for the Purcell's swimmer. In Proceedings of the 2017 IEEE/RSJ International Conference on Intelligent Robots and Systems (IROS), Vancouver, BC, Canada, 24–28 September 2017; pp. 3246–3251.
15. Giraldi, L.; Martinon, P.; Zoppello, M. Controllability and optimal strokes for N-link microswimmer. In Proceedings of the 52nd IEEE Conference on Decision and Control, Firenze, Italy, 10–13 December 2013; pp. 3870–3875.
16. Ramasamy, S.; Hatton, R.L. Soap-bubble optimization of gaits. In Proceedings of the IEEE 55th Conference on Decision and Control (CDC), Las Vegas, NV, USA, 12–14 December 2016; pp. 1056–1062. [\[CrossRef\]](#)
17. Wiezel, O.; Or, Y. Using optimal control to obtain maximum displacement gait for Purcell's three-link swimmer. In Proceedings of the 2016 IEEE 55th Conference on Decision and Control (CDC), Las Vegas, NV, USA, 12–14 December 2016; pp. 4463–4468.
18. Alouges, F.; DeSimone, A.; Giraldi, L.; Or, Y.; Wiezel, O. Energy-optimal strokes for multi-link microswimmers: Purcell's loops and Taylor's waves reconciled. *New J. Phys.* **2019**, *21*, 043050. [\[CrossRef\]](#)
19. Ramasamy, S.; Hatton, R.L. The Geometry of Optimal Gaits for Drag-Dominated Kinematic Systems. *IEEE Trans. Robot.* **2019**, *35*, 1014–1033. [\[CrossRef\]](#)
20. Wiezel, O.; Ramasamy, S.; Justus, N.; Or, Y.; Hatton, R.L. Geometric analysis of gaits and optimal control for three-link kinematic swimmers. *Automatica* **2023**, *158*, 111223. [\[CrossRef\]](#)
21. Deng, S.; Cowan, N.; Bittner, B. Adaptive Gait Modeling and Optimization for Principally Kinematic Systems. In Proceedings of the IEEE 2024 International Conference on Robotics and Automation (ICRA), Yokohama, Japan, 13–17 May 2024; pp. 12571–12577. [\[CrossRef\]](#)
22. Gutman, E.; Or, Y. Symmetries and gaits for Purcell's three-link microswimmer model. *IEEE Trans. Robot.* **2016**, *32*, 53–69. [\[CrossRef\]](#)
23. Passov, E.; Or, Y. Dynamics of Purcell's three-link microswimmer with a passive elastic tail. *Eur. Phys. J. E Soft Matter Biol. Phys.* **2012**, *35*, 78. [\[CrossRef\]](#)
24. Alouges, F.; Desimone, A.; Giraldi, L.; Zoppello, M. Can Magnetic Multilayers Propel Artificial Microswimmers Mimicking Sperm Cells? *Soft Robot.* **2015**, *2*, 117–128. [\[CrossRef\]](#)
25. Alouges, F.; DeSimone, A.; Giraldi, L.; Zoppello, M. Purcell magneto-elastic swimmer controlled by an external magnetic field. *IFAC-Pap.* **2017**, *50*, 4120–4125. [\[CrossRef\]](#)
26. Grover, J.; Vedova, D.; Jain, N.; Travers, M.; Choset, H. Motion Planning, Design Optimization and Fabrication of Ferromagnetic Swimmers. In Proceedings of the Robotics: Science and Systems (RSS), Breisgau, Germany, 22–26 June 2019; pp. 79–87.
27. Moreau, C. Local controllability of a magnetized Purcell's swimmer. *IEEE Control. Syst. Lett.* **2019**, *3*, 637–642. [\[CrossRef\]](#)
28. Zigelman, A.; Ben Zvi, G.; Or, Y. Dynamics of Purcell-type microswimmers with active-elastic joints. *Phys. Rev. E* **2024**, *110*, 014207. [\[CrossRef\]](#) [\[PubMed\]](#)
29. Serrano, A.J.; Nuevo-Gallardo, C.; Traver, J.E.; Tejado, I.; Vinagre, B.M. Purcell's three-link microswimmer based on IPMC: Simulations in COMSOL Multiphysics. *IEEE Lat. Am. Trans.* **2022**, *20*, 474–480. [\[CrossRef\]](#)
30. Traver, J.E.; Nuevo-Gallardo, C.; Rodríguez, P.; Tejado, I.; Vinagre, B.M. Modeling and control of IPMC-based artificial eukaryotic flagellum swimming robot: Distributed actuation. *Algorithms* **2022**, *15*, 181. [\[CrossRef\]](#)
31. Shahinpoor, M.; Kim, K.J. Ionic polymer–metal composites: IV. Industrial and medical applications. *Smart Mater. Struct.* **2004**, *14*, 197. [\[CrossRef\]](#)
32. Bonomo, C.; Brunetto, P.; Fortuna, L.; Giannone, P.; Graziani, S.; Strazzeri, S. A Tactile Sensor for Biomedical Applications Based on IPMCs. *IEEE Sens. J.* **2008**, *8*, 1486–1493. [\[CrossRef\]](#)
33. Rapp, B.E. *Microfluidics: Modelling, Mechanics and Mathematics*; Elsevier: Amsterdam, The Netherlands, 2017.
34. Alexander, D.E. *Nature's Machines*; Elsevier: Amsterdam, The Netherlands, 2017.
35. Nelson, B.J.; Kaliakatsos, I.K.; Abbott, J.J. Microrobots for Minimally Invasive Medicine. *Annu. Rev. Biomed. Eng.* **2010**, *12*, 55–85. [\[CrossRef\]](#)
36. Happel, J.; Brenner, H. *Low Reynolds Number Hydrodynamics*, 2nd ed.; Martinus Nijhoff Publishers: Leiden, The Netherlands, 1983. [\[CrossRef\]](#)
37. White, F.M. *Fluid Mechanics*, 7th ed.; Mc Graw-Hill: New York, NY, USA, 2011.
38. Lauga, E.; Powers, T.R. The hydrodynamics of swimming microorganisms. *Rep. Prog. Phys.* **2009**, *72*, 096601. [\[CrossRef\]](#)
39. Traver, J.E. Diseño de un Robot Nadador de Pequeñas Dimensiones tipo Flagelo eucariótico Artificial. Aplicaciones Médicas. Ph.D. Thesis, University of Extremadura, Badajoz, Spain, 2023.
40. Pettersen, K.Y. Snake robots. *Annu. Rev. Control.* **2017**, *44*, 19–44. [\[CrossRef\]](#)
41. Nuevo-Gallardo, C.; Traver, J.E.; Tejado, I.; Vinagre, B.M. Purcell's Three-Link Swimmer: Assessment of Geometry and Gaits for Optimal Displacement and Efficiency. *Mathematics* **2021**, *9*, 1088. [\[CrossRef\]](#)
42. Kim, K.J.; Takodoro, S. *Electroactive Polymers for Robotic Applications*; Springer: Berlin/Heidelberg, Germany, 2007.
43. Bernat, J.; Gajewski, P.; Kołota, J.; Marcinkowska, A. Review of Soft Actuators Controlled with Electrical Stimuli: IPMC, DEAP, and MRE. *Appl. Sci.* **2023**, *13*, 1651. [\[CrossRef\]](#)
44. Tejado, I.; Traver, J.E.; Prieto-Arranz, J.; López, M.Á.; Vinagre, B.M. Frequency Domain Based Fractional Order Modeling of IPMC Actuators for Control. In Proceedings of the 18th European Control Conference (ECC), Naples, Italy, 25–28 June 2019; pp. 4112–4117.

45. MohdIsa, W.; Hunt, A.; HosseinNia, S.H. Sensing and Self-Sensing Actuation Methods for Ionic Polymer–Metal Composite (IPMC): A Review. *Sensors* **2019**, *19*, 3967. [[CrossRef](#)] [[PubMed](#)]
46. Jiang, J.; Lin, C.; Xu, S.; Yu, Y.; Yao, L.; Huang, Z. Application-Oriented Modeling of Soft Actuator Ionic Polymer–Metal Composites: A Review. *Adv. Intell. Syst.* **2024**, *6*, 2300568. [[CrossRef](#)]
47. 3DM Advanced Materials, 3DM-TOUGH Resin. Available online: <https://www.3dm-shop.com/product-page/3DM-TOUGH> (accessed on 3 September 2024).
48. De Luca, V.; Digiamberardino, P.; Di Pasquale, G.; Graziani, S.; Pollicino, A.; Umana, E.; Xibilia, M.G. Ionic electroactive polymer metal composites: Fabricating, modeling, and applications of postsilicon smart devices. *J. Polym. Sci. Part B Polym. Phys.* **2013**, *51*, 699–734. [[CrossRef](#)]
49. Hunt, A.; Freriks, M.; Sasso, L.; Esfahani, P.M.; HosseinNia, S.H. IPMC Kirigami: A Distributed Actuation Concept. In Proceedings of the 2018 International Conference on Manipulation, Automation and Robotics at Small Scales (MARSS), Nagoya, Japan, 4–8 July 2018; pp. 1–6.
50. Hunt, A.; Chen, Z.; Tan, X.; Kruusmaa, M. Control of an inverted pendulum using an Ionic Polymer–Metal Composite actuator. In Proceedings of the IEEE/ASME International Conference on Advanced Intelligent Mechatronics, AIM, Montreal, QC, Canada, 6–9 July 2010; pp. 163–168.
51. Nuevo Gallardo, C. Robots Nadadores tipo Purcell: Alternativas de Diseño y Estrategias de Locomoción. Ph.D. Thesis, University of Extremadura, Badajoz, Spain, 2024.
52. Bay, H.; Ess, A.; Tuytelaars, T.; Van Gool, L. Speeded-Up Robust Features (SURF). *Comput. Vis. Image Underst.* **2008**, *110*, 346–359. [[CrossRef](#)]

Disclaimer/Publisher’s Note: The statements, opinions and data contained in all publications are solely those of the individual author(s) and contributor(s) and not of MDPI and/or the editor(s). MDPI and/or the editor(s) disclaim responsibility for any injury to people or property resulting from any ideas, methods, instructions or products referred to in the content.